ISSN 1674-1056
http://cpb.iphy.ac.cn
http://iopscience.iop.org/cpb
中国物理 B
Chinese Physics
中国物理
Chinese Physics B

UAV flight test of plasma slats and ailerons with microsecond dielectric barrier discharge

Zhi Su(苏志), Jun Li(李军), Hua Liang(梁华), Bo-Rui Zheng(郑博睿), Biao Wei(魏彪), Jie Chen(陈杰), Li-Ke Xie(谢理科)
Citation: Chin. Phys. B . 2018, 27(10): 105205. **doi:** 10.1088/1674-1056/27/10/105205

Journal homepage: http://cpb.iphy.ac.cn; http://iopscience.iop.org/cpb

What follows is a list of articles you may be interested in

Effect of actuating frequency on plasma assisted detonation initiation

Si-Yin Zhou(周思引), Xue-Ke Che(车学科), Di Wang(王迪), Wan-Sheng Nie(聂万胜)
Chin. Phys. B . 2018, 27(2): 025208. **doi:** 10.1088/1674-1056/27/2/025208

Modeling and optimization of the multichannel spark discharge

Zhi-Bo Zhang(张志波), Yun Wu(吴云), Min Jia(贾敏), Hui-Min Song(宋慧敏), Zheng-Zhong Sun(孙正中), Ying-Hong Li(李应红)
Chin. Phys. B . 2017, 26(6): 065204. **doi:** 10.1088/1674-1056/26/6/065204

Electric and plasma characteristics of RF discharge plasma actuation under varying pressures

Huimin Song(宋慧敏), Min Jia(贾敏), Di Jin(金迪), Wei Cui(崔巍), Yun Wu(吴云)
Chin. Phys. B . 2016, 25(3): 035204. **doi:** 10.1088/1674-1056/25/3/035204

Simulation of transition from Townsend mode to glow discharge mode in a helium dielectric barrier discharge at atmospheric pressure

Li Xue-Chen, Niu Dong-Ying, Xu Long-Fei, Jia Peng-Ying, Chang Yuan-Yuan
Chin. Phys. B . 2012, 21(7): 075204. **doi:** 10.1088/1674-1056/21/7/075204

Experimental investigation of nanosecond discharge plasma aerodynamic actuation

Wu Yun,Li Ying-Hong,Jia Min,Liang Hua,Song Hui-Min
Chin. Phys. B . 2012, 21(4): 045202. **doi:** 10.1088/1674-1056/21/4/045202

UAV flight test of plasma slats and ailerons with microsecond dielectric barrier discharge*

Zhi Su(苏志)[1], Jun Li(李军)[1], Hua Liang(梁华)[1,†], Bo-Rui Zheng(郑博睿)[2,‡], Biao Wei(魏彪)[1], Jie Chen(陈杰)[1], and Li-Ke Xie(谢理科)[1]

[1] *Science and Technology on Plasma Dynamics Laboratory, Air Force Engineering University, Xi'an* 710038, *China*
[2] *School of Automation and Information, Xi'an University of Technology, Xi'an* 710048, *China*

(Received 10 May 2018; revised manuscript received 25 July 2018; published online 10 September 2018)

Plasma flow control (PFC) is a promising active flow control method with its unique advantages including the absence of moving components, fast response, easy implementation, and stable operation. The effectiveness of plasma flow control by microsecond dielectric barrier discharge (μs-DBD), and by nanosecond dielectric barrier discharge (NS-DBD) are compared through the wind tunnel tests, showing a similar performance between μs-DBD and NS-DBD. Furthermore, the μs-DBD is implemented on an unmanned aerial vehicle (UAV), which is a scaled model of a newly developed amphibious plane. The wingspan of the model is 2.87m, and the airspeed is no less than 30m/s. The flight data, static pressure data, and Tufts images are recorded and analyzed in detail. Results of the flight test show that the μs-DBD works well on board without affecting the normal operation of the UAV model. When the actuators are turned on, the stall angle and maximum lift coefficient can be improved by 1.3° and 10.4%, and the static pressure at the leading edge of the wing can be reduced effectively in a proper range of angle of attack, which shows the ability of μs-DBD to act as plasma slats. The rolling moment produced by left-side μs-DBD actuation is greater than that produced by the maximum deflection of ailerons, which indicates the potential of μs-DBD to act as plasma ailerons. The results verify the feasibility and efficacy of μs-DBD plasma flow control in a real flight and lay the foundation for the full-sized airplane application.

Keywords: plasma flow control, flight test, dielectric barrier discharge, UAV

PACS: 52.30.–q, 47.85.Ld, 47.20.Ib, 47.32.Ff **DOI:** 10.1088/1674-1056/27/10/105205

1. Introduction

Flow separation is an important problem which is widely concerned in aviation. Once the flow over aircraft has been separated properly, great lift will be lost and drag will increase. Therefore, the control of flow separation is important for the better performance of aircraft.[1–4]

Plasma flow control (PFC) is a promising active flow control method with fast response, simple structure, and broad frequency band, and able-to-suppress the boundary layer separation effectively.[5–8] Since Roth first employed One Atmosphere Uniform Glow Discharge Surface Plasma as boundary layer separation control devices,[9] a large number of researches dealing with dielectric barrier discharge (DBD) actuators have been conducted.[9–25] The DBD actuators driven by alternating-current high-voltage (AC-DBD) are studied most.[12–17] The stall angle of an NACA 0015 wing model can be improved by 7° at a freestream velocity of 30 m/s with AC-DBD.[17] The DBD actuators driven by nanosecond pulses can concentrate their power in several to tens of nanoseconds and create the rapid localized heating of the gas layer near the surface,[20] which has a good flow control performance with Mach number up to 0.74.[18–25] Although the flow control effect[16] and the global flow response[25] of AC-DBD and NS-DBD are similar, and the question remains over which of them is better, there is a great potential for the NS-DBD in separation control. However, the NS-DBD may generate severe electromagnetic interference (EMI) and disable other devices (like computers, servo motors, and flight control systems) without being properly protected. Whether such actuators can be used in real flight and whether they work well without destroying the airborne equipment is still unknown. Therefore, flight tests are necessary to verify the feasibility of PFC before putting it into practical application.

Several flight tests using AC-DBD as the flow control method have been reported. Sidorenko applied AC-DBD to a real flight in 2008, but the results of flow control were not explicit.[26] In 2009, Grundman compared the stall speed of an unmanned aerial vehicle (UAV) between plasma actuation on and off by the statistical method and verified the control efficacy of AC-DBD.[27] In 2014, Friedrichs built a PFC flight testing platform and introduced the process in detail, but no result of the flight test was given.[28] In 2016, Zhang conducted a UAV flight test with AC-DBD plasma flow control. The variation of roll angle and the static pressure of the lead-

*Project supported by the National Natural Science Foundation of China (Grant Nos. 51336011 and 51607188), the China Postdoctoral Science Foundation (Grant No. 2014M562446), and the PhD Research Startup Foundation of Xi'an University of Technology (Grant No. 256081802).

†Corresponding author. E-mail: lianghua82702@tom.com
‡Corresponding author. E-mail: 527059665@qq.com

© 2018 Chinese Physical Society and IOP Publishing Ltd

ing edge were recorded and analyzed.[29] So far, the airspeed in the flight tests is within 20 m/s, and the flight altitude is low, which is very different from the conditions of real planes. Meanwhile, there are only qualitative results or preliminary quantitative results to show the efficacy of PFC in flight, and no flight test is conducted with DBD actuators driven by high-voltage pulses (pulsed-DBD) like NS-DBD which has good flow control performance from low speed ($Ma \leq 0.1$)[21,25] to the high subsonic conditions ($Ma = 0.74$).[18] To pave the way to the practical application, more comprehensive and quantitative data of flight tests must be acquired, and the feasibility of pulsed-DBD in real flight needs to be proved.

In the present study the typical NS-DBD is modified with a pulse rising time of several-to-tens of nanoseconds by relaxing the pulse rising time to 700 ns to remit the EMI. The pulse rising time of these modified pulses is close to 1 μs so the actuators driven by these pulses are defined as microsecond dielectric barrier discharge (μs-DBD) actuators. In this paper, the flow control ability of μs-DBD and typical NS-DBD are compared in the wind tunnel tests. The μs-DBD is applied to a real flight with a scaled model of a certain type of amphibious plane to study its practical application efficacy. The airspeed of the scaled model is larger than 30 m/s. In this process, a miniaturized microsecond high-voltage pulse generator is designed to feed the actuators and fit the limited cabin capacity of the scaled model. Abundant flight attitude data, wing pressure data together with tufts images are recorded and analyzed systematically to demonstrate the flow control efficacy comprehensively.

2. Experimental setup

2.1. Flight testing model

A scaled model of a certain type of amphibious plane is chosen as a flight testing model, as shown in Fig. 1. Figure 1(a) shows the arrangement of the airborne facilities while figure 1(b) shows the coordinate setup of the model. The wingspan of the model is 2.87 m, and the root chord length is 0.4 m. When looking down towards the model, the inner part of its main wing is of a rectangle with the airfoil section of NACA 23018, and the outer part is of an isosceles trapezoid. The airfoil section of the outer part is of smooth transition from NACA 23018 to NACA 4412 that is the airfoil section of the wing tip. The maximum load of the model is 8 kg, and its center of gravity is 40% chord length from the leading edge. The slats are replaced by the μs-DBD plasma actuators to verify the efficacy of μs-DBD to delay stall. The elevators, rudders, and ailerons are controlled remotely, while the flaps in the inner part and middle of the wing are fixed with no deflection. The maximum deflection of the ailerons is ±20°. The model is a glider carried by a transport plane and released at an altitude of 1600 m. The airspeed of the model is larger than 30 m/s.

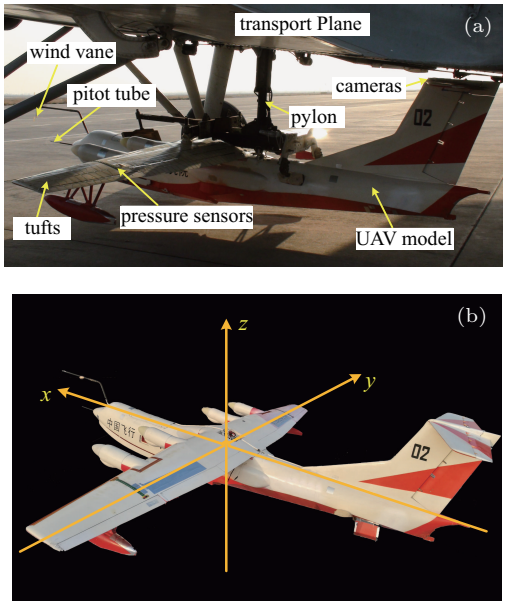


Fig. 1. (color online) Scaled model showing (a) arrangement of airborne facilities and (b) coordinate setup.

2.2. DBD plasma actuator

The DBD plasma actuator consists of two copper electrodes separated by a dielectric barrier with no overlap, as illustrated in Fig. 2(a). The electrodes are both 0.1 mm in depth while the exposed electrode is 3 mm in width and the covered electrode is 5 mm in width. The dielectric barrier is made of 3 layers of Kapton tapes which in total are 0.2 mm in depth. The total length of the actuators is 2 m. According to previous researches,[22,24] with the actuators located at various chordwise positions of the wing, it has a better flow control effect when the actuator is located at the leading edge than when the actuators located at the middle of the wing or on the trailing edge. To make it easier to locate the actuator and simplify the processing techniques in future application, the junction between

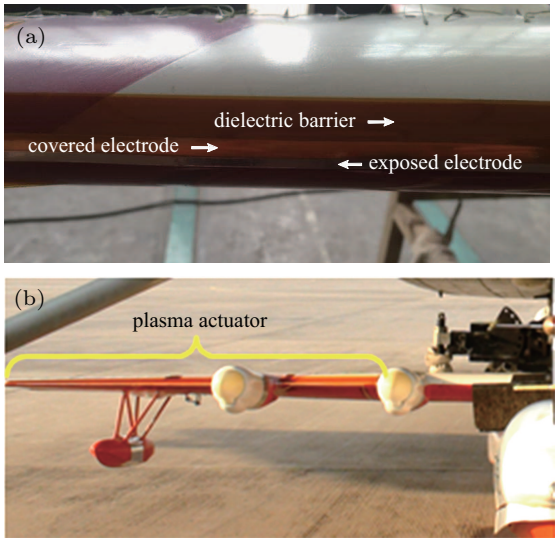


Fig. 2. (color online) DBD plasma actuator, showing (a) configuration and (b) location of plasma actuator.

the two electrodes of the actuator is located right on the leading edge. The actuators are placed at the outer parts of the wing to provide a greater rolling moment for rolling control and simulate the ailerons as shown in Fig. 2(b).

2.3. Microsecond high-voltage pulse generator

The cabin capacity of the scaled model is limited within 0.01 m^3 and batteries are the only power supply in the model. So, a specialized small-sized high-voltage generator is designed to generate the microsecond high-voltage pulses on board as shown in Fig. 3. The generator is divided into four parts, and each part can be located in different cabins of the UAV. The length, width, and height of each part demonstrated in Table 1 result in the total volume and weight of 0.0066 m^3 and 4 kg. The generator is driven by a 6 S battery with a capacity of 5000 mAh. Previous studies show that the best flow control effect can be achieved when the reduced frequency $F^+ = (f \times c)/V_\infty \approx 1$.[22–24] The f, c, and V_∞ represent the pulse frequency, mean aerodynamic chord length, and freestream velocity respectively. So, the pulse frequency is set to be 100 Hz to ensure $F^+ \approx 1$. The pulse rising time and the peak to peak value of the pulse voltage of the output pulse are 700 ns and 10 kV, as shown in Fig. 4. The cabin of the high-voltage generator is wrapped with aluminum foil to diminish the radiated EMI.

Table 1. The sizes of different parts of microsecond high-voltage pulse generator.

Serial number	Length/m	Width/m	Height/m	Volume/m^3	Weight/kg
Part 1	0.25	0.22	0.06	0.0033	2.1
Part 2	0.25	0.12	0.04	0.0012	0.8
Part 3	0.25	0.12	0.04	0.0012	0.3
Part 4	0.17	0.10	0.05	0.00085	0.8

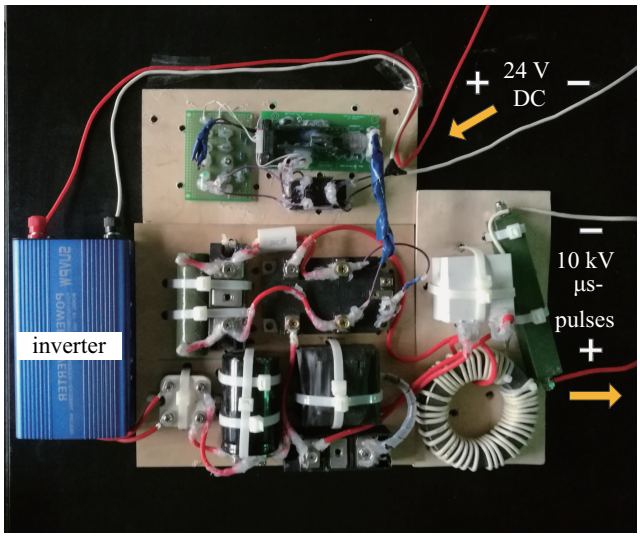


Fig. 3. (color online) Microsecond high-voltage pulse generator.

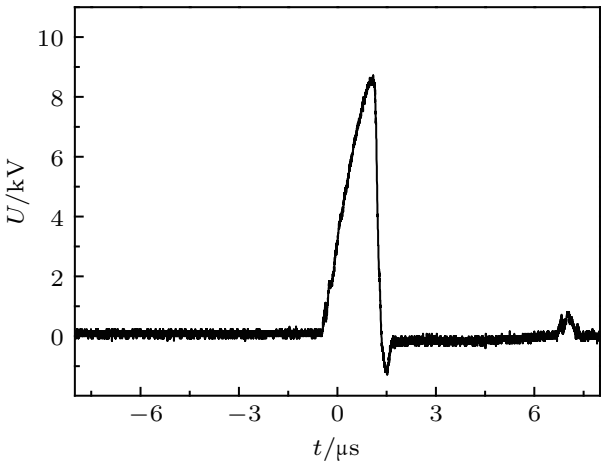


Fig. 4. Voltage waveform of a microsecond pulse.

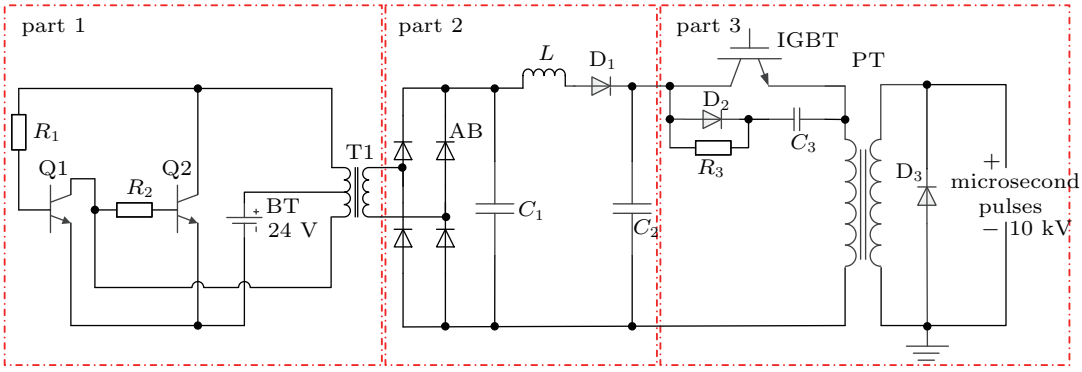


Fig. 5. (color online) Circuit of microsecond high-voltage pulse generator.

The circuit of the high-voltage generator consists of three parts, as shown in Fig. 5. The direct-current (DC) voltage provided by the battery is increased once in each part and eventually converted into a microsecond high-voltage pulse. The first part of the generator is an inverter, which converts the 24-V DC voltage into 220-V alternating-current (AC) voltage. Following that, the second part stabilizes the 220-V AC into 310-V DC with an electric bridge and a capacitor C_1 and charges the capacitor C_2. The third part of the generator has an insulated gate bipolar transistor (IGBT) semiconductor switch, which can be turned on and off periodically. Whenever the IGBT turns on, it will be turned off in a very short time. Thus,

the pulses each with a pulse rising time of a few hundred nanoseconds are formed by the periodical discharge of capacitor C_2 under the control of the IGBT. However, the amplitude for each of these pulses is only several hundred volts. So a pulse transformer PT is adopted to increase the voltage amplitude to 10 kV. The IGBT is turned on and off every 10 ms, producing a pulse frequency of 100 Hz. Finally, the high-voltage pulses are trimmed by a diode D_3 to wipe out negative pulses and then ignite the actuators.

2.4. Measuring methods

Two circuit boards equipped with fourteen MS5611-01BA03 static pressure sensors on each board are placed chordwise with 0.47 m from the wing tip on either side of the wing because there is the largest variation of static pressure before and after actuation at that airfoil section. The first sensor is 35 mm away from the leading edge, and the distance between adjacent sensors is 10 mm for the 1st to 12th sensors and 15 mm for the 12th to 14th sensors as shown in Fig. 6 with yellow spots representing the sensors. The measuring range of the pressure sensors is from 1 kPa to 120 kPa, and their error is less than 0.01 kPa. The sampling frequency for each of these sensors is 1 Hz. Besides, the AP202 automatic flight control system (AFCS) of the scaled model is equipped with diverse sensors and various flight attitude data including the overload, roll angle, roll angular velocity, etc. can be acquired. A pitot tube together with a wind vane is installed in front of the aircraft nose. So, the airspeed can be measured by the pitot tube and the angles of attack, and the sideslip angle can be measured by the wind vane. Furthermore, the upper surface of the wing is covered with tufts, and two cameras, each of which faces to one side of the wing, are attached on the vertical fin as shown in Fig. 1(a). Thus, the tufts' images of the whole process can be recorded to show the flow separation condition. The measuring equipment mentioned above cannot transmit the data to the ground during the flight. They can only record the data. The data recorded will be downloaded after the model has landed.

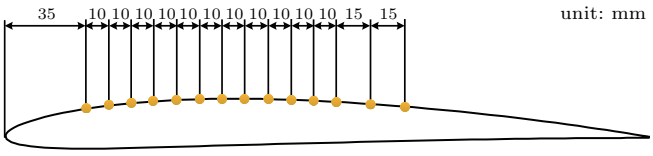


Fig. 6. (color online) Distribution of pressure sensors.

3. Results and discussion

3.1. Wind tunnel test

According to the Maxwell equation, fluctuation of voltage and current can produce an electromagnetic wave. For the airborne devices, the electromagnetic wave also means EMI. The shorter the pulse rising time, the stronger the EMI will be due to the stronger fluctuation of pulse voltage.[30,31] Thus, to alleviate EMI, the pulse rising time of NS-DBD is relaxed from a few nanoseconds to tens of nanoseconds to about one microsecond, producing the discharge called μs-DBD. Although the EMI is reduced, it is not sure whether this method of increasing pulse rising time will damage the flow control effect. So, the flow control effects of μs-DBD and NS-DBD with pulse rising time of 700 ns and 10 ns respectively are compared with a typical NACA 0015 airfoil in the wind tunnel test.

The test is conducted in a low-speed wind tunnel at Air Force Engineering University with a typical NACA 0015 airfoil as shown in Fig. 7. The facility is a closed-return wind tunnel possessing a square test section with a length and height of 1 m and width of 1.2 m. The chord length of the airfoil is 0.25 m, and the span is set to be 1.2 m to avoid the wing tip effect. The maximum freestream velocity of the wind tunnel is 75 m/s, and the turbulence intensity is below 0.2%. In the wind tunnel test, the airspeed is set to be 30 m/s. The static pressure at the surface of the airfoil is measured by 74 pressure taps at the middle span of the model with a pressure scanner. The range and sampling frequency of the scanner are ±11 kPa and 100 Hz with an accuracy better than 0.1% F.S. The values of lift coefficient (Cl) at different values of the angle of attack (α) are calculated with the mean value of pressure data recorded for 6 s by the scanner in the wind tunnel test.

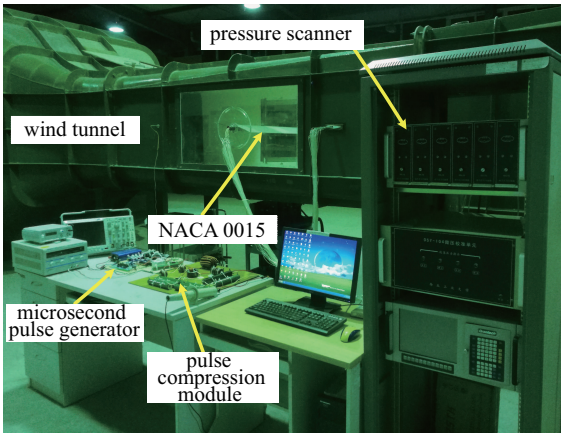


Fig. 7. (color online) Wind tunnel test setup.

The small-sized microsecond pulse generator and a nanosecond pulse generator that generates pulses with a pulse rising time of 10 ns are used in the wind tunnel test to make a comparison. The output waveform of the nanosecond pulse generator is shown in Fig. 8. The peak to peak value of the pulse voltage and pulse frequency are set to be 10 kV and 100 Hz, respectively. The nanosecond pulses are produced by compressing the microsecond pulses with a pulse compression module as shown in Fig. 9. In this module, two magnetic switches are included. When the magnetic switch is saturated, the current of the switch will reverse sharply. This

effect can be used to compress the pulses. The microsecond pulses are compressed once in each magnetic switch and become nanosecond pulses to ignite the actuators.

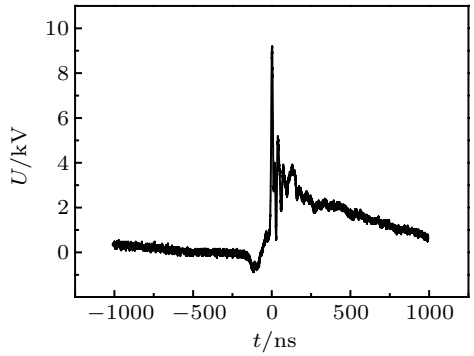


Fig. 8. Voltage waveform of a nanosecond pulse.

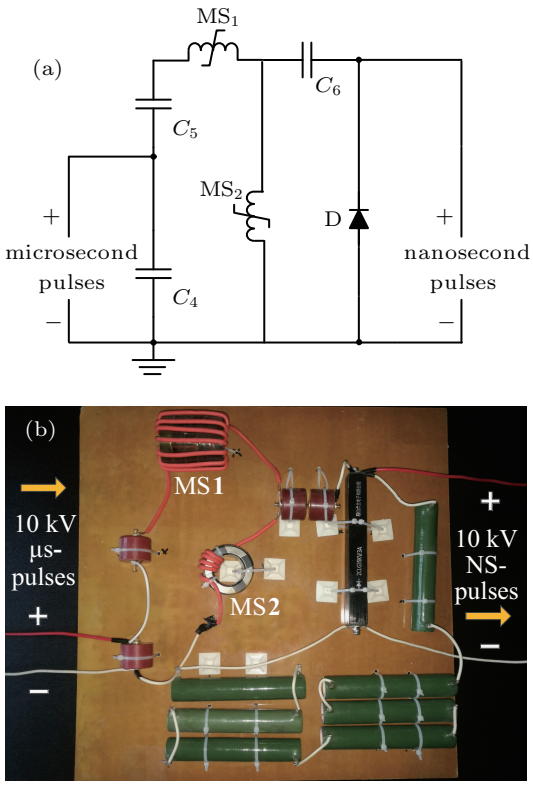


Fig. 9. (color online) Pulse compression module, showing (a) circuit and (b) photograph of the pulse compression module.

The lift coefficient curves and pressure distributions of the airfoil with and without plasma actuation are compared in Fig. 10, where x means the location of the pressure taps and p represents the static pressure of the airfoil. When the plasma actuator is off, the lift coefficient rises with the increase of the angle of attack, reaching a maximum value at a stall angle of 12°, and then decreases sharply due to severe flow separation. The suction peak at $\alpha = 13°$ is small due to the flow separation. When the actuator is turned on, the lift coefficient right after the stall angle increases dramatically and the suction peak rises due to the subdued separation produced by plasma actuation. The stall angle is delayed by 1° both with NS-DBD and μs-DBD. The lift enhancement and pressure variation caused by NS-DBD and μs-DBD are almost the same, which indicates that μs-DBD has flow control ability comparable to the flow control ability that NS-DBD has at a freestream velocity of 30 m/s, while the EMI of μs-DBD is much weaker than that of NS-DBD due to the larger pulse rising time. Therefore, the μs-DBD is used in the flight test to balance the flow control effect and the radiated EMI.

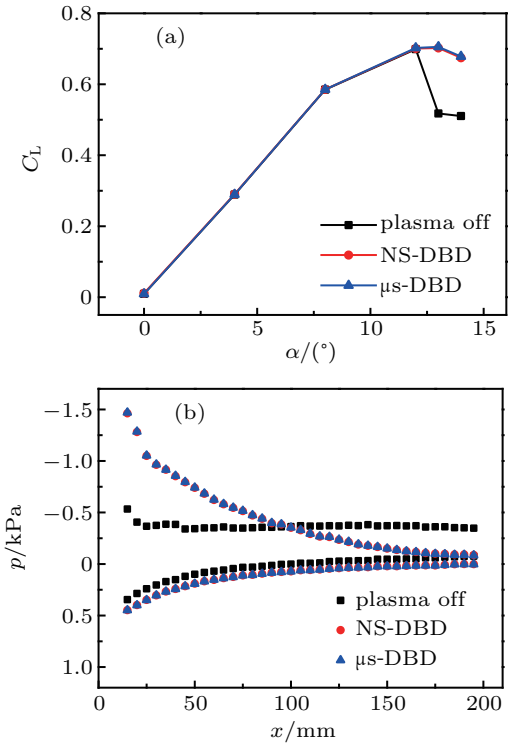


Fig. 10. (color online) Comparison between flow control effects with NS-DBD and μs-DBD, showing (a) lift coefficient curves and (b) pressure distribution curves at $\alpha = 13°$.

3.2. Flight test

To verify the practical application capability of μs-DBD and simulate the function of typical slats and ailerons, flight tests of μs-DBD with two actuation configurations are conducted. Firstly, actuators on either side of the wing are turned on, which is called bilateral actuation. Then, the actuator at the left wing is turned on, which is named left-side actuation. The bilateral actuation configuration is designed to demonstrate the overall lift enhancement, stall delay, and pressure variation of the wing surface caused by the plasma actuation, which is similar to the function of typical slats. The left-side actuation configuration aims to highlight the control of varying the roll angle of plasma actuation through flight attitude change and to verify the capability of μs-DBD actuators to act as plasma ailerons in real flight. When the actuator of the left wing is turned on, the lift of the left wing will be improved, but the lift of the right wing is still the same, which will produce a rolling moment and make the model roll to the right.

During the flight test, the model is adjusted to level flight right after being released. Then, the plasma actuation is turned on. The model is controlled to increase its angles of attack gradually with bilateral actuation or left-side actuation. When

the model stalls due to a large angle of attack, it is controlled to pitch down quickly and recovers to level flight. The model can pitch up and down four times before it reaches an altitude of 600 m where the plasma actuation is turned off. When the model continues gliding and reaches an altitude of 400 m, the parachute is opened, and the model lands slowly. The remote control and servo motors are slightly interfered by the μs-DBD during the flight, but this does not affect the normal operation of the whole aircraft.

3.2.1. Lift coefficient analysis

Based on the overload (n), angle of attack, density of the air (ρ), and airspeed (v) recorded by the AFCS, together with the mean aerodynamic chord (c_a) and the weight (W) of the UAV model, the lift coefficient of the model can be calculated with the following equation acquired with force analysis:

$$C_L = \frac{-Wn_x \sin\alpha + Wn_z \cos\alpha}{\frac{1}{2}\rho v^2 \times c_a}, \quad (1)$$

where n_x and n_z are the overload in the axial direction (x) and vertical direction (z) shown in Fig. 1(b) respectively. Both the data points of the lift coefficient calculated, and the lift coefficient curves acquired by polynomial fitting are shown in Fig. 11. The baseline statistics are acquired from the clean wing before any actuator is applied.

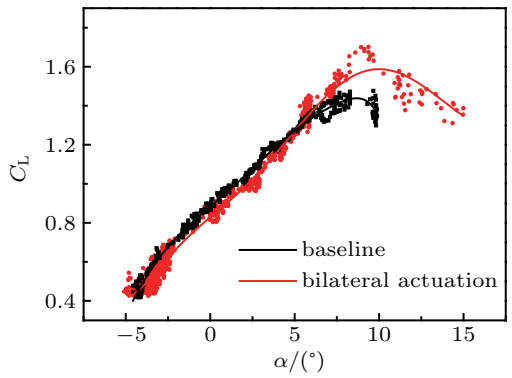


Fig. 11. (color online) Plots of lift coefficient versus angle of attack in the cases with and without plasma actuation in flight.

When the angle of attack is less than 5°, the lift coefficient of the baseline increases linearly with the angle of attack and the lift coefficient with bilateral actuation is slightly less than that of the baseline condition. This is because no conspicuous flow separation exists at such an angle of attack, and the lift coefficient cannot be improved by plasma actuation through separation control. However, the shape of the airfoil leading edge is changed slightly because of the presence of plasma actuators and deviates from the designed condition, which causes the lift loss. When the angle of attack is greater than 5°, the growth of lift coefficient turns slower, and the lift coefficient reaches a maximum value at the stall angle $\alpha_{stall} = 8.7°$ due to severe flow separation without plasma actuation. After that, the lift coefficient drops sharply and the UAV model stalls. When the actuators on both sides are turned on, the flow separation is suppressed effectively, and the lift coefficient increases substantially. The stall angle and maximum lift coefficient are increased by 1.3° and 10.4%, respectively, which shows a remarkable flow control performance of μs-DBD in real flight. Such a phenomenon is similar to the effect of typical slats so the bilateral μs-DBD actuator is defined as plasma slats. The μs-DBD actuator has a simpler structure, better flexibility, and it is much easier to achieve closed-loop control than with the mechanical slats.

3.2.2. Flight attitude analysis

To verify the rolling control capability of μs-DBD and show the lift enhancement generated by plasma actuation in an intuitional way, test groups with left-side actuation are implemented and flight data including angle of attack, roll angle (ϕ), roll angular velocity (ω), and deflection of ailerons (δ) are recorded. During the tests, the UAV model operates in the automatic trim mode, in which the ailerons will deflect automatically, trying to keep the roll angle at about 0°. The flight attitude variations of a typical test group are shown in Fig. 12, and the corresponding tufts' images are shown in Fig. 14. The positive roll angle and angular velocity represent the UAV model rolling to the right and the positive deflecting angle of ailerons represents the right aileron deflecting upward and left aileron deflecting downward, which can produce a positive rolling moment. Results with the left-side actuation show the sound flow control performance of μs-DBD. The great rolling moment can be generated by the μs-DBD actuation on the left side of the wing. The moment produced by μs-DBD is larger than that produced by the maximum deflection of ailerons when the angle of attack is kept at an appropriate value. Hence, the μs-DBD has the potential to act as an alternate flight control device which can strengthen or even replace the ailerons of UAVs in the appropriate range of angle of attack and is defined as plasma ailerons.

The variation for each of flow separation condition and rolling moment with the change of angle of attack in a typical test group can be divided into six stages. The time point of $t = 717.5$ s when the model begins to increase its angle of attack is taken as t_0. The six stages are divided with yellow dash–dotted lines in Fig. 12. The process of a typical test group is illustrated as follows.

When the time is smaller than $t_0 + 4.3$ s ($t_0 \le t < t_0 + 4.3$ s), the angle of attack is smaller than 8° ($\alpha < 8°$). The flow separation is weak, and the lift losses caused by the separation are relatively small. The plasma actuation cannot produce considerable lift improvement by suppressing flow separation, so the lift on each side of the wing is nearly the same. The lift difference between the two sides of the wing can be offset easily by the moderate deflection of ailerons. Therefore, the model keeps flying horizontally and the aileron deflecting angle fluctuates gently around 0°.

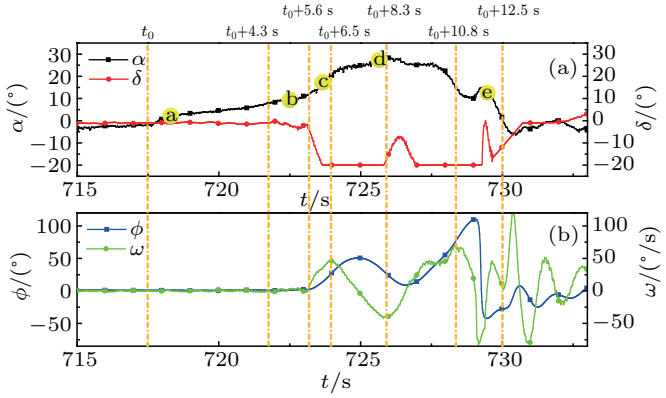


Fig. 12. (color online) Variations of flight attitude with left-side actuation.

In the time period from $t_0+4.3$ s to $t_0+5.6$ s ($t_0+4.3$ s$\leq t < t_0+5.6$ s), the angle of attack becomes larger ($8^\circ \leq \alpha < 12^\circ$), and considerable flow separation appears. The separation on the left wing is controlled by the μs-DBD but it is still uncontrolled at the right wing. Thus, the lift of the left wing becomes greater than that of the right wing and a rightward rolling moment M_{plasma} is formed, which results in a positive roll angular velocity. To balance M_{plasma} and return to horizontal flight, the ailerons obtain negative deflection, which produces a revising moment M_{aileron}. In this condition, the separation becomes noticeable but the rolling moment M_{plasma} produced by the left-side actuation can still be revised when the deflection of ailerons turns larger. As a result, the fluctuation of roll angular velocity and aileron deflection becomes a bit violent while the roll angle keeps about 0°. In the process, the negative deflection of ailerons increases gradually, which means that the flow separation keeps aggravating and M_{plasma} keeps rising, and thus requiring larger aileron deflection for balance.

In the time period from $t_0+5.6$ s to $t_0+6.5$ s ($t_0+5.6$ s$\leq t < t_0+6.5$ s), the angle of attack increases to 12° ($12^\circ \leq \alpha < 21^\circ$). Flow separation turns serious, leading to the significant lift loss. The M_{plasma} rises sharply and keeps larger than M_{aileron} though the ailerons reach a maximum deflecting angle of −20° rapidly for revising at $t = 723.6$ s$= t_0+6.1$ s. The ailerons can no longer revise M_{plasma} on this condition. Both the roll angle and angular velocity rise quickly, and the UAV model speeds up rolling positively. The great rolling moment is generated by the μs-DBD actuation on the left side of the wing. The moment produced by μs-DBD is larger than that produced by the maximum deflection of ailerons, which shows the potential of μs-DBD plasma actuators to strengthen or replace the ailerons and improve the maneuverability as well as simplify the aircraft in an appropriate range of angles of attack ($12^\circ \leq \alpha < 21^\circ$ in this test).

In the time period from $t_0+6.5$ s to $t_0+8.3$ s ($t_0+6.5$ s$\leq t < t_0+8.3$ s), the angle of attack becomes much larger ($21^\circ \leq \alpha < 28.7^\circ$), reaching a maximum value of 28.7° at $t = 725.8$ s$= t_0+8.3$ s. The flow separation becomes severe and much more difficult to control. The μs-DBD can no longer suppress the separation effectively, which makes M_{plasma} decrease significantly. As a result, M_{plasma} turns smaller than M_{aileron} with the aileron deflection being a maximum value. The roll angular velocity decreases and the positively rolling slows down. When $t = 724.9$ s$= t_0+7.4$ s, the model stops rolling positively with a roll angle of 50.8° and begins to roll negatively.

In the time period from $t_0+8.3$ s to $t_0+10.8$ s ($t_0+8.3$ s$\leq t < t_0+10.8$ s), the aileron deflection begins to decrease because of the negative rolling and reaches a minimum value of −7.1°, which makes M_{aileron} decrease significantly. The angle of attack also begins to decrease, and the flow separation becomes alleviated. The μs-DBD regains the ability to enhance the lift, and causes M_{plasma} to rise. Thus, M_{plasma} becomes larger than M_{aileron} again. The roll angular velocity begins to increase, and the negatively rolling slows down. At $t = 726.6$ s$= t_0+9.1$ s, the model begins to roll positively, and the aileron deflection increases to a maximum value again to resist the positive rolling. However, because M_{plasma} keeps increasing with the decrease of the angle of attack, it has become larger than the maximum value of M_{aileron} at that time. So, the model speeds up rolling with the maximum aileron deflection again.

When the time is larger than $t_0+10.8$ s ($t_0+10.8$ s$\leq t < t_0+12.5$ s), the angle of attack drops sharply. The separation recedes and becomes mild. M_{plasma} disappears while M_{aileron} still keeps negative. The positive rolling slows down, reaching a maximum roll angle of 110.3° at $t = 729$ s$= t_0+11.5$ s. Then, the ailerons try to adjust the model to horizontal flight from the huge roll angle of 110.3°, causing the roll angle and angular velocity to greatly fluctuate. Finally, the roll angle returns to 0° at $t = 730$ s$= t_0+12.5$ s, and the flight model recovers to horizontal flight. The whole process is described in Fig. 13.

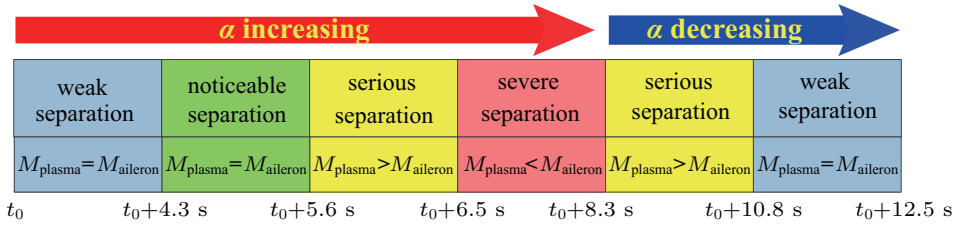


Fig. 13. (color online) Different stages of test group with left-side actuation.

3.2.3. Tufts image analysis

As shown in Fig. 14, the tufts' images demonstrate the flow field condition of the process illustrated in Fig. 12. Each of the images in Fig. 14 is seamed with two photos recorded by the two cameras on the vertical fin. Because of the different viewing angles of the cameras, the fuselage and the sweep angle of the wing are distorted. However, this does not influence the analyses of the tufts. The corresponding angles of attack of the tufts' images are marked as yellow spots in Fig. 12, and the roll angle is demonstrated with a sketch map of the UAV model on the right side of each image. The results are as follows.

When $\alpha < 8^\circ$, nearly all the tufts are straight and attached to the wing surface as indicated in Fig. 14(a), which indicates that no obvious separation exists. The roll angle keeps at 0° and the aileron deflecting angle fluctuates gently around 0°.

When $8^\circ \leq \alpha < 12^\circ$, a considerable flow separation appears, and the separation condition of the left wing is better than that of the right wing due to the left-side actuation. This can be seen from the tufts at the outer part of the wing. Most of the tufts at the left wing are attached while those at the right wing are erect, as shown in Fig. 14(b). The tufts at the middle parts are submerged by the reflection of sunlight, so the flow condition at those parts cannot be observed clearly.

When $12^\circ \leq \alpha < 21^\circ$, serious asymmetric separation happens under the left-side actuation and the flight model begins to roll to the right. The positive roll angular velocity gives a downward velocity component to the incoming flow of the left wing and makes the local angle of attack of the left wing decrease. The incoming flow of the right wing obtains an upward velocity component, making the local angle of attack of the right wing increase. For the left wing, the local angle of attack is small, so that the separation can be easily suppressed by the plasma actuation. Most of the tufts of the left wing are attached. For the right wing, the local angle of attack is large, and the plasma actuator there is turned off. Thus, the separation there is serious and cannot be suppressed. As a result, the tufts of the right wing are upright and wobbly. The combined influence of left-side plasma actuation and the different local angles of attack between two sides of the wing produce the different separation conditions. The ailerons obtain a maximum negative deflection to resist the rolling, as shown in Fig. 14(c).

When $21^\circ \leq \alpha < 28.7^\circ$, the angle of attack reaches a maximum value and the μs-DBD loses the ability to suppress separation. The rightwards rolling slows down and the model begins to roll to the left, which makes the local angle of attack of the left wing increase and that of the right wing decrease. Thus, the boundary layer of the left wing becomes separated, and much more difficult to control due to the large local angle of attack, while that of the right wing becomes attached due to the small local angle of attack. The tufts of the left wing become erect, but part of the tufts of the right wing are attached due to the combined effect of local angles of attack and plasma actuation, as shown in Fig. 14(d).

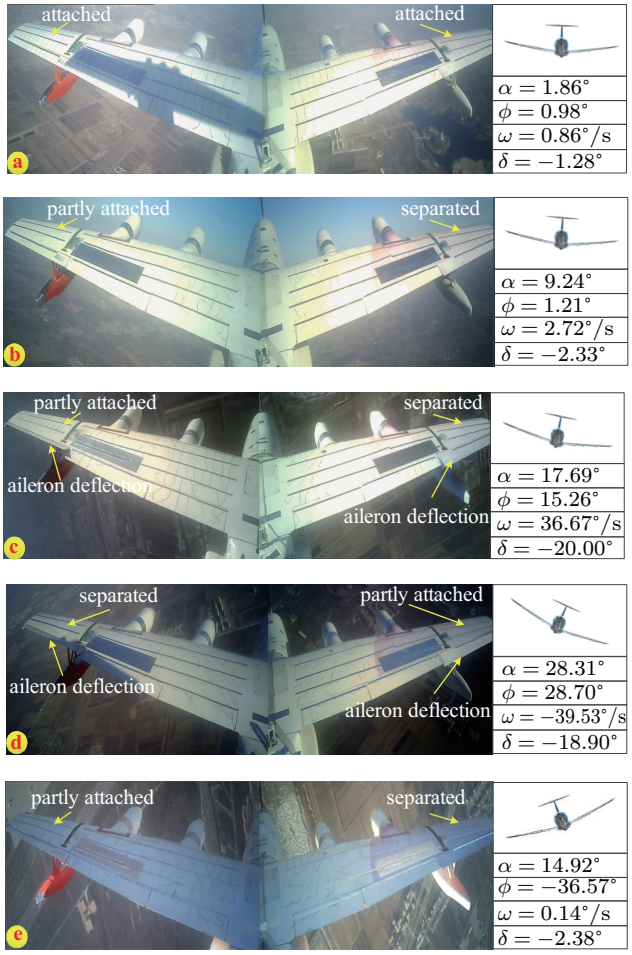


Fig. 14. (color online) Tufts' images with left-side actuation at (a) $\alpha \leq 8^\circ$, (b) $8^\circ \leq \alpha < 12^\circ$, (c) $12^\circ \leq \alpha < 21^\circ$, (d) $21^\circ \leq \alpha < 28.7^\circ$, and (e) angles of attack decreasing.

When the angle of attack begins to decrease, the μs-DBD regains the flow control authority. The separation at the left wing is suppressed again, and the rightwards rolling reappears. The tufts of the left wing are attached while those at the right wing are upright, as shown in Fig. 14(e). This phenomenon is similar to that happening under the condition of $12^\circ \leq \alpha < 21^\circ$. Then, the ailerons try to make the model recover the level flight, thus causing the roll angle and angular velocity to fluctuate significantly.

3.2.4. Wing pressure analysis

Tufts' images can only qualitatively display the flow field. To assess the flow field more quantitatively, the static pressure of the wing surface is recorded and analyzed.

The pressure variations in the cases with and without actuation of the first pressure sensor p_1 at either side of the wing are shown in Fig. 15. The variations of static pressure at either side of the wing are similar, while the pressure of the right wing is a little smaller than that of the left wing. This is caused

by the slight difference between the locations of the two circuit boards equipped with pressure sensors and the difference in the auxiliary equipment between the two sides of the wing. When the angle of attack is small, the pressure at either side drops quickly at $\alpha \approx 3^\circ$ and keeps fluctuating at a relatively low value no matter whether the actuators are on or off. When the angle of attack turns larger, the flow control effect appears.

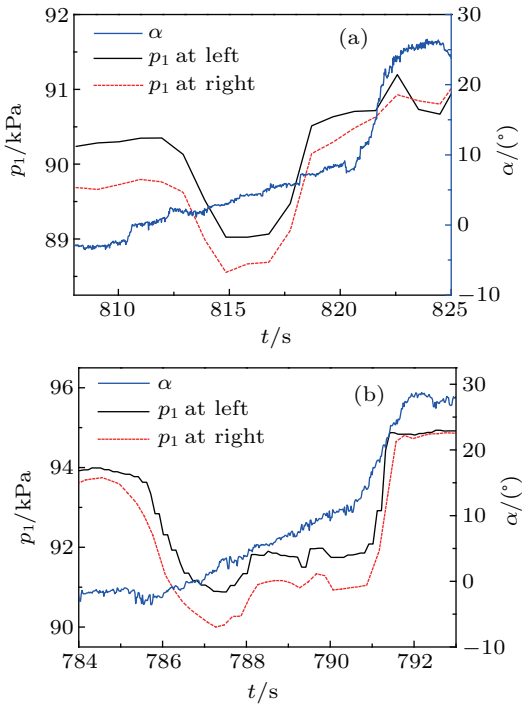


Fig. 15. (color online) Variations of pressure with time in the cases of (a) plasma off and (b) bilateral actuation.

With the actuators turned off, the pressure at either side begins to rise at $\alpha \approx 5^\circ$, which means that the static pressure at the surface of the airfoil profile with pressure sensors begins to increase and flow separation appears. When the angle of attack continues to increase, the pressure reaches a relatively high value at $\alpha \approx 15^\circ$ and keeps fluctuating around that value, which indicates that the airfoil falls into deep separation.

When the actuators on both sides are turned on, the pressure keeps at a relatively low value at $\alpha \approx 5^\circ$ and does not begin to rise until $\alpha \approx 14^\circ$. The pressure keeps at a relatively low value between $\alpha \approx 5^\circ$ and $\alpha \approx 14^\circ$. With the angle of attack increasing, the pressure reaches a relatively high value at $\alpha \approx 20^\circ$. The flow separation is suppressed effectively in an appropriate range of angle of attack ($5^\circ < \alpha < 14^\circ$). Because the static pressure variation of one point of the wing cannot represent the overall stall condition, the range of angle of attack in which the μs-DBD works is different from that in the lift coefficient analysis. However, this result can still reflect the efficacy of μs-DBD to act as plasma slats more quantitatively.

The pressure distribution of the wing surface is not acquired due to some unexpected problems with the pressure recording system. Following studies will fix this problem and make efforts to acquire more systematic pressure data.

4. Conclusions

In this paper, the flow control ability of μs-DBD is compared with that of typical NS-DBD in the wind tunnel tests and the feasibility and efficacy of μs-DBD are verified in the flight test with a scaled model of a certain type of amphibious plane. The wingspan of the model is 2.87 m, and the airspeed is no less than 30 m/s. During the tests, a miniaturized high-voltage generator with a volume and weight of 0.0066 m^3 and 4 kg is designed to fit the limited cabin capacity; the flight data, the wing pressure data, and the tufts' images are recorded and analyzed comprehensively.

The results show that the μs-DBD actuators work well in flight without influencing the overall operation of the aircraft and have good flow control performances both in the wind tunnel tests and flight tests. In the wind tunnel tests, the lift enhancement and pressure distribution improvement produced by the μs-DBD and NS-DBD are nearly the same with the stall angle increased by 1°. Thus, the μs-DBD is chosen in the flight test due to both its flow control ability being similar to the NS-DBD and the reduced EMI. In the flight test, the stall angle and maximum lift coefficient are increased by 1.3° and 10.4% with the μs-DBD, which shows the potential of μs-DBD actuators to delay the stall and act as the plasma slats in flight. Great asymmetric separation and the positive rolling moment are generated by the left-side μs-DBD actuation. The moment produced by the μs-DBD is larger than that produced by the maximum deflection of ailerons in an appropriate range of angle of attack ($12^\circ \leq \alpha < 21^\circ$), which demonstrates the ability of μs-DBD to act as plasma ailerons in real flight. Besides, the static pressure of the point at 47 cm away from the wing tip and 35 mm away from the leading edge decreases effectively in an appropriate range of angle of attack ($5^\circ < \alpha < 14^\circ$), which verifies the efficacy of μs-DBD to suppress the flow separation more quantitatively. With these results, the practical application capability of the μs-DBD is verified comprehensively in diverse perspectives.

The next flights are aimed to gain more flight data with larger Reynolds numbers and verify the ability of plasma actuators to act as circulation-control devices.

References

[1] Anderson J D 2014 *Fundamental of aerodynamics* (New York: McGraw Hill Book Company) pp. 381–398
[2] Greenblatt D and Wygnanski I 2000 *Prog. Aerosp. Sci.* **36** 487
[3] Gadelhak M 1991 *Asme Trans J. Fluids Eng.* **113** 5
[4] Lin J C 2002 *Prog. Aerosp. Sci.* **38** 389
[5] Jin D, Li Y H, Jia M, Li F Y, Cui W, Sun Q, Zhang B L and Li J 2014 *Chin. Phys. B* **23** 035201
[6] Sun Q, Cui W, Li Y H, Cheng B Q, Jin D and Li J 2014 *Chin. Phys. B* **23** 075210

[7] Cheng K and Liang H 2016 *Chin. Phys. B* **25** 024703
[8] Wang J J, Choi K S, Feng L H, Jukes T N and Whalley R D 2013 *Prog. Aerosp. Sci.* **62** 52
[9] Roth J R, Sherman D M and Wilkinson S P 1998 *36th AIAA Aerospace Sciences Meeting and Exhibit*, January 12–15, 1998, Reno, Nevada, AIAA 1998: 0328
[10] Corke T C, Ensole C L and Wilkinson S P 2010 *Ann. Rev. Fluid Mech.* **42** 505
[11] Li Y H, Wu Y and Li J 2012 *Int. J. Flow Control* **4** 1
[12] Roth J R, Sherman D M and Wilkinson S P 2000 *AIAA J.* **38** 1166
[13] Bernard N, Pons-Prats J, Periaux J, Bugeda G, Braud P, Bonnet J P and Moreau E 2016 *Exp. Fluid* **57** 1
[14] Greenblatt D, Kastantin Y, Nayeri C N and Paschereit C O 2008 *AIAA J.* **46** 1554
[15] Yang L, Li J, Cai J, Wang G and Zhang Z 2016 *J. Fluid Eng.* **138** 365
[16] Kelley C L, Bowles P O, Cooney J, He C, Corke T C, Osborne B A, Silkey J S and Zehnle J 2014 *AIAA J.* **52** 1871
[17] He C, Corke T C and Patel M P 2009 *J. Aircraft* **46** 864
[18] Roupassov D, Nikipelov A, Nudnova M and Starikovskii A 2009 *AIAA J.* **47** 168
[19] Little J, Takashima K, Nishihara M, Adamovich I and Samimy M 2012 *AIAA J.* **50** 350
[20] Little J, Takashima K, Nishihara M, Adamovich I and Samimy M 2010 *AIAA 5th Flow Control Conference*, AIAA 2010-4256
[21] Rethmel C, Little J, Takashima K, Sinha A, Adamovich I and Samimy M 2011 *49th AIAA Aerospace Sciences Meeting*, January 4–7, 2011, Orlando, Florida, AIAA 2011-487
[22] Han M H, Li J, Liang H, Niu Z G and Zhao G Y 2015 *Plasma Sci. Technol.* **17** 502
[23] Zhao G Y, Li Y H, Liang H, Hua W Z and Han M H 2015 *Acta Phys. Sin.* **64** 15101 (in Chinese)
[24] Wei B, Liang H, Niu Z G, Wang D B and Li Y H 2016 *High Voltage Engineering* **42** 782 (in Chinese)
[25] Durasiewicz C, Singh A and Little J 2018 *AIAA Aerospace Sciences Meeting*, 8–12 January, 2018, Kissimmee, Florida, AIAA 2018-1061
[26] Sidorenko A, Budovsky A, Pushkarev A and Maslov A 2006 *AIAA Aerospace Sciences Meeting & Exhibit* **24** 479
[27] Grundmann S, Frey M and Tropea C 2009 *47th AIAA Aerospace Sciences Meeting*, January 5–8, 2009, Orlando, Florida, AIAA 2009-698
[28] Friedrichs W 2014 *"Unmanned Aerial Vehicle for flow control experiments with dielectric barrier discharge plasma actuators"*, Ph. D. Dissertation (Darmstadt: Technical University of Darmstadt)
[29] Zhang X, Huang Y, Yang P Y, Zhang P, Huang Z Y, Wang D W and Li H X 2018 *Acta Aeronautica Astronautica Sin.* **39** 121587 (in Chinese)
[30] Zhou H A, Du Z W and Gong K 2005 *High Power Laser and Particle Beams* **17** 783 (in Chinese)
[31] Guo H X, Zhou H, Chen Y S, Zhang Y M, Gong R X, Guan Y, Han F B and Gong J C 2002 *Microelectronics & Computer* **3** 17 (in Chinese)